Contact Interaction Analysis of a Sliding Bearing Sleeve with Friction and Separation Zones in an Elastic Layer

UDC:621.822.1:539.3
Original scientific paper https://doi.org/10.46793/adeletters.2026.5.1.3

Vitaly Miroshnikov[1*], Serhii Sverdlov[1], Olexii Ilyin[1], Mykhailo Kosenko[1], Iaroslav Grebeniuk[1], Basheer Yunis[1], Nataliia Ukrayinets[1]

[1]National Aerospace University "Kharkiv Aviation Institute", Kharkiv, Ukraine

Abstract:
This paper investigates the contact interaction in a sliding bearing assembly modeled as a system comprising an elastic layer (polymer or composite housing), a press-fit steel sleeve (bushing), and a rigid shaft — a configuration representative of bearing nodes in lightweight aircraft and mechanical engineering structures. The research determines the stress-strain state of this assembly under imperfect-contact conditions, explicitly accounting for partial-contact zones (regions of sleeve-shaft separation arising from elastic deformation of the housing under transverse loading) and dry-friction forces. The method employs the generalized Fourier method combined with an adaptive iterative algorithm based on alternating boundary conditions to resolve the nonlinear contact problem with unknown contact boundaries. Unlike classical approaches that assume full contact, the proposed model correctly identifies the extent of the partial contact zone and the redistribution of contact pressure as a function of load direction and friction coefficient. The results demonstrate rapid convergence (3–4 iterations) and provide accurate stress and displacement distributions for use in the strength assessment and geometric optimization of sliding bearing assemblies.

ARTICLE HISTORY
Received: 2 February 2026
Revised: 9 March 2026
Accepted: 17 March 2026
Published: 31 March 2026

KEYWORDS
Sliding bearing, Partial contact, Friction contact, Layer with cylindrical inclusion, Stress-strain state, Lamé equation, Generalized Fourier method

1. INTRODUCTION

Modern aircraft and mechanical engineering structures increasingly employ sliding bearing assemblies in which a steel bushing is press-fitted into a polymer — a configuration that combines low weight with high local stiffness at fastening and pivot nodes. Under transverse operational loads, elastic deformation of the compliant housing causes partial separation of the bushing from the shaft, creating a zone of lost contact that full-contact models fail to capture, thereby underestimating peak stresses in the bearing zone. Accurate determination of the partial-contact zone boundaries, contact pressure redistribution, and the influence of dry friction is essential for service life prediction, fatigue prevention, and geometry optimization of such assemblies. This challenge is particularly relevant to the objectives of the European Flightpath 2050 program [1] regarding structural safety and damage tolerance.

The creation of modern aviation and mechanical engineering structures requires combining massive load-bearing elements with reinforcing components. Kondratiev and Kovalenko [2] noted that optimizing the design parameters of such systems, in particular composite fairings, is key to ensuring their efficiency under power and thermal loads. Continuing this theme, Kondratiev [3] focuses on improving the weight efficiency of main fairings through the use of sandwich structures, which requires accurate methods for calculating their strength. In study [4], the authors deepen the analysis by examining the influence of layer orientation on the mechanical characteristics of honeycomb fillers, thereby emphasizing the

*CONTACT: Vitaly Miroshnikov, e-mail: v.miroshnikov@khai.edu

importance of considering material anisotropy and microstructure in computational models.

Special attention must be paid to tribological aspects, as surface roughness and lubrication conditions significantly influence the friction coefficient, a fact emphasized in recent research by Vicen et al. [5].

Accurate determination of contact interaction parameters, including contact pressure distribution and friction forces, remains a fundamental challenge in the mechanics of solids [6]. Quaglini et al. [7] developed a constitutive law describing the dependence of the friction coefficient of polymers on contact pressure during sliding on metal surfaces, confirming that, for self-lubricating polymers in sliding bearings, the friction coefficient depends significantly on the load. The problem of sliding contact with friction on compliant surfaces has also been studied analytically by Menga et al. [8], who obtained solutions for a rigid surface sliding over a viscoelastic half-space, confirming the strong influence of friction on contact pressure redistribution. However, the complexity of contact geometry often requires a combination of approaches. Ivanović et al. [9] emphasized the importance of comparative analyses between analytical and numerical calculations of contact stresses to ensure the reliability of the results.

The transition from general design solutions to the analysis of local areas, such as fastening nodes or bearing connections, requires the use of more complex mathematical tools. Traditionally, numerical methods are used for this purpose. Thus, Gontarovskyi et al. [10] demonstrate the effectiveness of numerical analysis of fuel tanks in a three-dimensional setting. The importance of correctly determining the elastic properties of materials, in particular rubber-metal elements, for the accuracy of such calculations is substantiated in the work of Golovanevskiy and Kondratiev [11].

Further research by Gontarovskyi et al. [12] shows that the finite element method (FEM) allows for detailed analysis of bimetallic shells and verification of theoretical models. The expansion of the scope of application of FEM is demonstrated in the work of Jafari et al. [13], where numerical algorithms are used to minimize thermal stresses in perforated plates. A common limitation of the numerical approaches discussed [10–13], despite their universality, is that FEM has limitations when modeling contact problems with an unknown contact area. Discretization of the domain introduces errors in the singularity zones of stresses, and modeling of infinite domains (layers) requires artificial limitation of the model size.

Alongside classical FEM, alternative numerical approaches, in particular domain decomposition and meshless methods, are actively used to solve elasticity contact problems.

Domain decomposition methods, described in detail in the works of Toselli and Widlund [14] and in the studies of Boucard and Ladevèze [15], enable the effective solution of large-scale problems by dividing the initial domain into subdomains and subsequently matching solutions at the boundaries. Although modern algorithms such as FETI (Finite Element Tearing and Interconnecting) demonstrate high efficiency in parallel computing, their application to contact problems with friction is often complicated by problems of convergence of iterative processes at interaction interfaces and the need to discretize each subdomain, which maintains the high computational cost of the problem [16].

Mesh-free methods, such as the element-free Galerkin (EFG) method or the local Petrov-Galerkin (MLPG) method, developed in the works of Atluri and Shen [17] and Belytschko et al. [18], eliminate the need to construct a finite element mesh, which is critical for problems involving large deformations or crack propagation.

An alternative is the use of analytical methods, which provide accurate results. In the work of Zasovenko and Fasolyak [19], a mathematical model of the dynamics of an elastic half-space with a cylindrical cavity reinforced by a shell was constructed. Malits [20] obtained an exact solution to the problem of torsion of a half-space with a cylindrical notch stamped out. Fundamental aspects of the equilibrium of a finite cylinder under the action of discontinuous loads are discussed in the work of Meleshko and Tokovyy [21], and Fesenko [22] provided an exact solution to the dynamic problem for a layer with a cylindrical cavity. The local problem in analytical work [19–22] is that these studies are mostly limited to either dynamic formulations or relatively simple boundary conditions, without accounting for the complex contact interactions characteristic of bearing assemblies (separation, friction).

Analytical and numerical approaches have also been applied to study stress concentrations in planar bodies with geometric discontinuities. Nikolić et al. [23] obtained the stress distribution in an anisotropic plane field weakened by an elliptical hole, demonstrating the sensitivity of stress concentration to material anisotropy. Radojković

et al. [24] further investigated the influence of the elliptical opening position on the principal stress distribution in rectangular plates, using both analytical solutions and FEM verification in ANSYS.

The most promising for the class of "layer–cylindrical inclusion" problems is the generalized Fourier method, described in detail in the monograph by Nikolaev and Protsenko [25].

Further development of the method focused on complicating the geometry and loads. In research [26], the stress state of a composite in the form of a layer and a half-space with a longitudinal cavity was investigated. In research [27], an approach was developed to account for spatially infinite loads in the "layer-cavity" system. The influence of non-classical mixed boundary conditions on the stress-strain state of a layer was analyzed by Grebenikov and Mironov [28].

A special group consists of works that consider the presence of inclusions (pipes, bearings). The study [29] considers the problem of rotation of a layer with a cylindrical pipe around a rigid cylinder, but the contact was considered ideal. In research [30], a layer with a cylindrical pipe was analyzed at given stresses on all boundary surfaces. The influence of the cylindrical gasket material on the stress-strain state of a layer with embedded supports was studied in the work of Miroshnikov et al. [31]. Finally, in [32], a step was taken to take into account the contact interaction for a layer with two pipes, but limited to the case of smooth contact without friction.

Analysis of closely related works [29–32] reveals a lack of comprehensive solutions for the 'elastic layer – pipe – shaft' system that simultaneously account for shaft detachment (incomplete contact) and friction forces.

The primary challenge lies in the mathematical complexity of combining the multi-connectivity of the region (a layer with a hole and inclusion) with the nonlinearity of the boundary conditions. The presence of unknown contact boundaries (partial contact zones) and the coexistence of stick and slip regions governed by Coulomb's friction law make the problem structurally nonlinear, which prevents the direct application of classical Fourier method schemes and necessitates the development of special iterative procedures.

2. PURPOSE AND OBJECTIVES OF THE STUDY

The aim of this study is to develop an analytical-numerical method for solving the spatial contact problem in elasticity theory for a multiply connected region and to identify the patterns of stress-strain distribution in the "elastic layer-pipe" system when interacting with a rigid shaft, taking into account separation zones and friction forces.

To achieve this aim, the following objectives were established:

1. Constructed a mathematical model of the spatial problem of elasticity theory for a layer rigidly connected to a cylindrical pipe, with mixed boundary conditions on the outer surfaces (stress on the upper boundary, displacement on the lower boundary) and smooth contact conditions on the inner surface of the pipe.
2. Obtained an analytical solution to the problem using the generalized Fourier method, which allowed obtaining stress and displacement fields in the form of a series of eigenfunctions for each of the regions.
3. Developed and implemented an iterative algorithm for refining contact interaction, based on sequential changes in the type of boundary conditions on the inner surface of the pipe (zeroing tensile stresses in the first stage and adjusting displacements in the "run-up" zones in the second stage) to model unilateral contact.
4. Performed a numerical analysis of the results obtained and investigated the distribution of stresses on the pipe surfaces depending on the specified load parameters and friction coefficient.

3. MATERIALS AND METHODS

The physical system under study represents a sliding bearing assembly of the type used in lightweight aircraft structures and mechanical engineering: an elastic layer (E_o = 1700 MPa, ν_o = 0.38) models a polymer housing — the adopted constants correspond to ABS engineering plastic; a steel sleeve (E_1 = 200000 MPa, ν_1 = 0.3) is press-fitted into the housing bore with zero nominal radial clearance, serving as the bearing bushing; the rigid shaft represents a high-stiffness metal rod whose compliance is negligible relative to the polymer housing. The absence of initial radial clearance is consistent with standard interference-fit tolerances for press-fitted bushings (e.g., H7/p6 fit class per ISO 286 [33]), which are widely adopted in both general mechanical engineering and aerospace structural assemblies. Under transverse loading, the elastic deformation of the polymer housing causes partial separation of the bushing inner surface from the shaft — a physically admissible effect that constitutes the central phenomenon of this study. The friction model at

the bushing–shaft interface corresponds strictly to dry friction conditions governed by the classic Amontons-Coulomb law, characterizing direct contact between the surfaces without the presence of a lubricating film. According to the literature, the typical friction coefficient for this contact ranges from *f*=0.04 to 0.1. However, values of *f*=0.1 and *f*=0.3 were adopted in the numerical study to conservatively simulate worst-case static breakaway conditions.

Assumptions made in the work:

1. The materials of the layer and the pipe were considered to be perfectly elastic, homogeneous, and isotropic, and their behaviour obeyed Hooke's law. This linear-elastic and isotropic approximation provides reliable conservative upper-bound stress estimates for typical polymer housings under standard operational loads, serving as a baseline before introducing material nonlinearity or anisotropy.
2. The case of small deformations was considered, which allowed the use of linear elasticity theory.
3. The shaft was considered to be a perfectly rigid body.

Simplifications adopted in the work:

1. The problem was considered in a steady-state setting (no inertial forces). Additionally, thermal expansions were neglected. The assumption of isothermal conditions is acceptable for assemblies operating at moderate, stable temperatures with no significant internal heat generation.
2. The contact surfaces were assumed to have ideal geometry. Surface roughness was neglected because its amplitude is negligible compared to the sleeve radius (R_1 =7 mm). This idealized smooth contact yields the nominal macroscopic stress state, which can be used as input data for future micro-level tribological models.

The study is based on the fundamental equations of spatial elasticity theory (Lamé equations) in curvilinear coordinates. Two coordinate systems are used to describe the geometry of the problem: Cartesian (*x, y, z*) to describe the stress-strain state of the layer (Fig. 1) and cylindrical (ρ, φ, z) to describe the pipe and the conditions on its surfaces. These coordinate systems are combined and oriented identically.

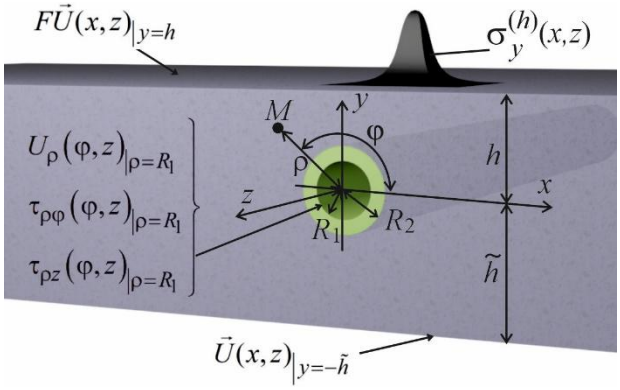

Fig. 1. Layer with a cylindrical pipe

The main analytical tool was the generalized Fourier method. To satisfy the boundary conditions at the interfaces (layer-pipe coupling), addition theorems for cylindrical functions are applied, which allows the solutions in different coordinate systems to be linked.

A stress vector was specified at the upper boundary of the layer, and a displacement vector was specified at the lower boundary of the layer:

$$F\vec{U}(x,z)_{|y=h} = \vec{F}_h^0(x,z), \vec{U}(x,z)_{|y=-\tilde{h}} = \vec{F}_{\tilde{h}}^0(x,z),$$

where:

$$\vec{F}_h^0(x,z) = \tau_{yx}^{(h)}\vec{e}_x + \sigma_y^{(h)}\vec{e}_y + \tau_{yz}^{(h)}\vec{e}_z, \qquad (1)$$

$$\vec{F}_{\tilde{h}}^0(x,z) = U_y^{(\tilde{h})}\vec{e}_y + U_x^{(\tilde{h})}\vec{e}_x + U_z^{(\tilde{h})}\vec{e}_z; \qquad (2)$$

where: $\vec{e}_x$, $\vec{e}_y$, $\vec{e}_z$ are orthogonal in the Cartesian coordinate system; $\tau_{yx}^{(h)}$, $\sigma_y^{(h)}$, $\tau_{yz}^{(h)}$, $U_y^{(\tilde{h})}$, $U_x^{(\tilde{h})}$, $U_z^{(\tilde{h})}$ are known functions.

At the interface between the layer and the pipe, the conditions of ideal mechanical contact (equality of displacement and stress vectors) are satisfied:

$$\vec{U}_0(\varphi,z)_{|\rho=R_2} = \vec{U}_p(\varphi,z)_{|\rho=R_2} \qquad (3)$$

$$F\vec{U}_0(\varphi,z)_{|\rho=R_2} = F\vec{U}_p(\varphi,z)_{|\rho=R_2} \qquad (4)$$

where: $\vec{U}_0(\varphi,z)$ is the solution for the layer; $\vec{U}_p(\varphi,z)$ is the solution for the pipe; $F\vec{U}$ is the stress operator.

Smooth contact conditions are specified on the inner surface of the pipe

$$\left.\begin{aligned} U_\rho(\varphi,z)_{|\rho=R_1} &= U_0^{(p)}(\varphi,z) \\ \tau_{\rho\varphi}(\varphi,z)_{|\rho=R_1} &= \tau_1^{(p)}(\varphi,z) \\ \tau_{\rho z}(\varphi,z)_{|\rho=R_1} &= \tau_2^{(p)}(\varphi,z) \end{aligned}\right\}, \quad (5)$$

which change during the iterative calculation process.

To account for the nonlinearity of contact (the presence of separation and friction zones), a special iterative algorithm of the Schwarz method type with alternating boundary conditions is implemented.

4. RESULTS OF RESEARCH ON THE CONTACT INTERACTION OF A SLIDING BEARING

4.1. Mathematical Formulation of the Spatial Problem for the "Layer-Tube-Shaft" System

Consider an elastic isotropic layer ($-\tilde{h} \le y \le h$) with elastic constants E_0 and ν_0, in which a cylindrical tube (bearing) with elastic constants E_1 and ν_1 is placed parallel to the boundaries. The pipe has an outer radius R_2 and an inner radius R_1 (Fig. 1).

To solve the problem, the approach described in study [29] was used, which is based on solving the Lamé equations under different boundary conditions. The displacement field for the layer and the pipe is constructed as a superposition of the basis solutions:

$$\vec{U}_0 = \sum_{k=1}^{3}\int_{-\infty}^{\infty}\sum_{m=-\infty}^{\infty} B_{k,m}(\lambda)\cdot\vec{S}_{k,m}(\rho,\varphi,z;\lambda)d\lambda + \\ +\sum_{k=1}^{3}\int_{-\infty}^{\infty}\int_{-\infty}^{\infty}\Big(H_k(\lambda,\mu)\cdot\vec{u}_k^{(+)}(x,y,z;\lambda,\mu) + \\ +\tilde{H}_k(\lambda,\mu)\cdot\vec{u}_k^{(-)}(x,y,z;\lambda,\mu)\Big)d\mu d\lambda, \quad (6)$$

$$\vec{U}_1 = \sum_{k=1}^{3}\int_{-\infty}^{\infty}\sum_{m=-\infty}^{\infty} A_{k,m}(\lambda)\cdot\vec{R}_{k,m}(\rho,\varphi,z;\lambda) + \\ +\tilde{A}_{k,m}(\lambda)\cdot\vec{S}_{k,m}(\rho,\varphi,z;\lambda)d\lambda, \quad (7)$$

where: $\vec{S}_{k,m}(\rho_p,\varphi_p,z;\lambda)$, $\vec{R}_{k,m}(\rho_p,\varphi_p,z;\lambda)$, $\vec{u}_k^{(+)}(x,y,z;\lambda,\mu)$ and $\vec{u}_k^{(-)}(x,y,z;\lambda,\mu)$ are the basis solutions given by Equations [25]:

$$\vec{u}_k^{\pm}(x,y,z;\lambda,\mu) = N_k^{(d)} e^{i(\lambda z+\mu x)\pm\gamma y}; \\ \vec{R}_{k,m}(\rho,\varphi,z;\lambda) = N_k^{(p)} I_m(\lambda\rho) e^{i(\lambda z+m\varphi)}; \\ \vec{S}_{k,m}(\rho,\varphi,z;\lambda) = N_k^{(p)} \times \\ \times\Big[(\operatorname{sign}\lambda)^m K_m(|\lambda|\rho)\cdot e^{i(\lambda z+m\varphi)}\Big]; k=1,2,3; \quad (8)$$

$N_1^{(d)} = \frac{1}{\lambda}\nabla$; $N_2^{(d)} = \frac{4}{\lambda}(\nu-1)\vec{e}_2^{(1)} + \frac{1}{\lambda}\nabla(y\cdot)$; $N_3^{(d)} = \frac{i}{\lambda}\operatorname{rot}\left(\vec{e}_3^{(1)}\cdot\right)$; $N_1^{(p)} = \frac{1}{\lambda}\nabla$; $\gamma = \sqrt{\lambda^2+\mu^2}$; $-\infty < \lambda,\mu < \infty$,

and the unknown functions $H_k(\lambda,\mu)$, $\tilde{H}_k(\lambda,\mu)$, $B_{k,m}(\lambda)$, $A_{k,m}(\lambda)$ and $\tilde{A}_{k,m}(\lambda)$ must be found from the boundary conditions (1) – (5); $I_m(\lambda\rho)$, $K_m(|\lambda|\rho)$ are Bessel functions.

Separate analytical solutions from (6) and (7), taking into account (8), to give an accurate result for their boundary surface.

To convert the basic solutions between coordinate systems, the following equations are used [25]:

- to transition from solutions $\vec{S}_{k,m}$ of the cylindrical coordinate system to solutions of the layer $\vec{u}_k^{(-)}$ (when y>0) and $\vec{u}_k^{(+)}$ (when y<0):

$$\vec{S}_{k,m}(\rho,\varphi,z;\lambda) = \frac{(-i)^m}{2}\int_{-\infty}^{\infty}\omega_{\mp}^m\cdot\vec{u}_k^{(\mp)}\cdot\frac{d\mu}{\gamma}, k=1,3; \\ \vec{S}_{2,m}(\rho,\varphi,z;\lambda) = \frac{(-i)^m}{2}\int_{-\infty}^{\infty}\omega_{\mp}^m\cdot\left(\left(\pm m\cdot\mu - \frac{\lambda^2}{\gamma}\right)\times\right. \quad (9) \\ \left.\times\vec{u}_1^{(\mp)} - \lambda^2\vec{u}_2^{(\mp)} \pm 4\mu(1-\nu)\vec{u}_3^{(\mp)}\right)\frac{d\mu}{\gamma^2},$$

where $\omega_{\mp}(\lambda,\mu) = \frac{\mu\mp\gamma}{\lambda}$, $m = 0,\pm1,\pm2,\ldots$;

- to transition from the solutions $\vec{u}_k^{(+)}$ and $\vec{u}_k^{(-)}$ of the layer to the solutions $\vec{R}_{k,m}$ of the cylindrical coordinate system [25]:

$$\vec{u}_k^{(\pm)}(x,y,z) = \sum_{m=-\infty}^{\infty}\left(i\cdot\omega_{\mp}\right)^m\vec{R}_{k,m}, (k=1,3); \\ \vec{u}_2^{(\pm)}(x,y,z) = \sum_{m=-\infty}^{\infty}\left[\left(i\cdot\omega_{\mp}\right)^m\cdot\frac{1}{\lambda^2}\left((m\cdot\mu)\times\right.\right. \quad (10) \\ \left.\left.\times\vec{R}_{1,m} \pm \gamma\cdot\vec{R}_{2,m} + 4\mu(1-\nu)\vec{R}_{3,m}\right)\right],$$

where:

$$\vec{R}_{k,m} = \vec{\tilde{b}}_{k,m}(\rho,\lambda)\cdot e^{i(m\varphi+\lambda z)};$$

$$\vec{\tilde{b}}_{2,n}(\rho,\lambda)=\vec{e}_\rho\cdot\left[(4\nu-3)\cdot I_n'(\lambda\rho)+\lambda\rho_p I_n''(\lambda\rho)\right]+$$

$$+\vec{e}_\varphi i\cdot m\left(I_n'(\lambda\rho)+\frac{4(\nu-1)}{\lambda\rho}I_n(\lambda\rho)\right)+\vec{e}_z i\lambda\rho I_n'(\lambda\rho);$$

$$\vec{\tilde{b}}_{3,n}(\rho,\lambda)=-\left[\vec{e}_\rho\cdot I_n(\lambda\rho)\frac{n}{\lambda\rho}+\vec{e}_\varphi\cdot i\cdot I_n'(\lambda\rho)\right],$$

where: $\vec{e}_\rho$, $\vec{e}_\varphi$, $\vec{e}_z$ are the orthogonals in the cylindrical coordinate system.

The sequence of solving this part of the problem differs little from [32], the only difference being in the given boundary conditions: boundary conditions (1), (2), and (5) are successively substituted into the corresponding Eqs. (6) and (7). This creates the first 9 infinite equations (three for each projection). Another 6 equations are created when the conjugation conditions (3) and (4) are satisfied. In total, 15 integro-algebraic equations are created to find 15 unknown solutions (6), (7). If, from the equations written for the flat surfaces of the layer, expressing $H_k(\lambda,\mu)$ and $\tilde{H}_k(\lambda,\mu)$ through $B_{k,m}(\lambda)$, and substituting them into other equations, 9 infinite algebraic equations are obtained of the second kind for finding the unknowns $B_{k,m}(\lambda)$, $A_{k,m}(\lambda)$ and $\tilde{A}_{k,m}(\lambda)$. After finding $B_{k,m}(\lambda)$ we find $H_k(\lambda,\mu)$ and $\tilde{H}_k(\lambda,\mu)$.

After determining the unknown coefficients of Eqs. (6) and (7), the stress and displacement of the inner surface of the pipe are determined.

4.2. Implementation of the Iterative Algorithm for Considering Delamination

As a result of solving the main problem (initial approximation), the stress state is obtained on the inner surface of the pipe ($\sigma_{\rho,n}^{(R_1)}$, with *n*=0 in the first calculation). At this stage, the possibility of separation was ignored. It was assumed that the pipe and the internal support (or shaft) are rigidly connected in the normal direction (the "adhesion" condition). That is, the contact is bilateral — it can transmit both compressive and tensile forces.

However, contact stresses can only be compressive ($\sigma_{\rho,0}^{(R_1)}\le 0$). The appearance of tensile stresses ($\sigma_{\rho,0}^{(R_1)}>0$) indicates physical separation of the pipe from the support, where the stresses should be zero.

A limitation of the generalized Fourier method is the condition of using only continuous functions on boundary surfaces, which requires the application of boundary conditions on each individual ortho of only one type — displacement or stress.

Friction condition: tangential stresses at the contact obey Coulomb's law and depend on normal pressure [6]: $\tau_{\rho\varphi}=\tau_{\rho z}=\mu_k\sigma_\rho$, where μ_k is the friction coefficient.

The contact problem is solved in the following sequence: (1) the linear problem with full bilateral contact is solved using the generalized Fourier method to obtain the initial stress-strain state; (2) zones of tensile contact stress are identified and designated as partial contact zones, where the boundary condition is switched to zero normal stress; (3) the updated problem is solved with Coulomb friction conditions applied in the remaining contact zones; (4) zones of non-physical interpenetration are eliminated by applying compensating contact pressure; (5) steps (2), (3) are repeated until convergence, which is achieved in 3–4 iterations. The detailed implementation of each step is described below.

Step 1. The first iteration consists of adjusting the boundary conditions based on the analysis of the stress state obtained from the linear problem. In areas where $\sigma_{\rho,0}^{(R_1)}>0$ separation occurs, the actual stress should become zero. In areas of compression ($\sigma_{\rho,0}^{(R_1)}\le 0$) contact is maintained.

Separation Criterion: The condition is checked $\sigma_{\rho,n}^{(R_1)}\le 0$ (compression or zero). In areas where tensile stresses have occurred ($\sigma_{\rho,n}^{(R_1)}$>0), these stresses are set to zero.

Approximation n=n+1. The problem is solved with the stresses $\sigma_{\rho,n}^{(R_1)}=-\frac{\left|\sigma_{\rho,n-1}^{(R_1)}\right|-\sigma_{\rho,n-1}^{(R_1)}}{2}$ specified on the inner surface of the pipe taking into account the friction coefficient in the contact zones (compression) $\tau_{\rho\varphi,n}^{(R_1)}=\left|\sigma_{\rho,n}^{(R_1)}\right|\cdot\mu_k$; $\tau_{\rho z,n}^{(R_1)}=\left|\sigma_{\rho,n}^{(R_1)}\right|\cdot\mu_k$. Since the new boundary condition functions are nonlinear and discontinuous (due to the modulus), to solve the problem using the generalized Fourier method, they must be decomposed into the basis functions of the problem. The obtained functions are transformed from physical space (*z, φ)* to the space of spectral coefficients (*m*, λ):

$$f_m(z)=\frac{1}{2\pi}\int_{-\pi}^{\pi} f(z,\varphi)e^{im\varphi}d\varphi;$$

$$F(m,\varphi)=\frac{1}{2\pi}\int_{-\infty}^{\infty} f(z)e^{i\lambda z}dz.$$

Since the problem is solved numerically, the integrals are replaced by Filon's quadrature formulas on a discrete grid of points λ_k. As a result, arrays of spectral coefficients are obtained, which are the right-hand sides for the system of linear algebraic equations of the additional problem. The system of linear algebraic equations is solved to obtain a new stress field $\sigma_{\rho,n}^{(R_1)}$ and displacement field $U_{\rho,n}^{(R_1)}$.

Step 2. As a result of the first iteration (using the elastic solution method), the contact force condition was satisfied: in areas of possible detachment, the normal tensile stresses were set to zero. However, this resulted in an error in the kinematic boundary conditions. Numerical analysis of the total displacement field $U_{\rho,n}^{(R_1)}$ showed the presence of areas where normal displacements on the contact surface are negative. From a physical point of view, this means "interpenetration" of bodies (the pipe "cuts into" the support/shaft), which is impossible for rigid or elastic contact.

Separation and penetration criterion: In the second iteration, it is necessary to eliminate the effect of mutual penetration by applying additional compensating contact pressures, returning the displacement to zero or to the positive region. We also check the condition $\sigma_{\rho,n}^{(R_1)}\le 0$ (compression or zero). In areas where tensile stresses have occurred ($\sigma_{\rho,n}^{(R_1)}$ >0), these stresses are zeroed.

Approximation n=n+1. It is necessary to press the surface to compensate for the negative displacement. A new problem is solved with the stresses specified on the inner surface of the pipe:

$$U_{\rho,n-1}^{(R_1)}\le 0,\ \sigma_{\rho,n}^{(R_1)}=\sigma_{\rho,n-1}^{(R_1)}+K_{eff}\cdot U_{\rho,n-1}^{(R_1)};\quad (11)$$

$$\sigma_{\rho,n-1}^{(R_1)}>0,\ \sigma_{\rho,n}^{(R_1)}=0;\quad (12)$$

$$U_{\rho,n-1}^{(R_1)}>0,\ \sigma_{\rho,n}^{(R_1)}=\sigma_{\rho,n-1}^{(R_1)},\quad (13)$$

where K_{eff} is the adaptive stiffness coefficient of the system, which is estimated as the ratio of the average stress to the average displacement: $K_{eff}=\left|\frac{\sum\sigma_{\rho,n-1}^{(R_1)}}{\sum U_{\rho,n-1}^{(R_1)}}\right|$. The stiffness coefficient is obtained based on the Fredholm integral equation of the first kind $U(M)=\iint G(M,P)\cdot P(P)d\Omega_P$ and is the "volume" of the stress diagram divided by the "volume" of the displacement diagram, which gives the average spring stiffness. The selection criterion K_{eff} is the maximum approximation of the values on the inner surface of the pipe to $U_{\rho,n}^{(R_1)}\ge 0$.

Adjusting the normal pressure entails a change in friction forces according to Coulomb's law. New target tangential stresses: $\tau_{\rho\varphi,n}^{(R_1)}=\left|\sigma_{\rho,n}^{(R_1)}\right|\cdot\mu_k$; $\tau_{\rho z,n}^{(R_1)}=\left|\sigma_{\rho,n}^{(R_1)}\right|\cdot\mu_k$. The principle of solving the problem is the same as in the previous step. As a result, a new stress field is obtained $\sigma_{\rho,n}^{(R_1)}$ and displacement field $U_{\rho,n}^{(R_1)}$.

Step 3. Contact problems are nonlinear. Two conditions are satisfied simultaneously, which influence each other. Applying new pressure could cause the pipe to bend, leading to new separation zones appearing at neighboring points where they did not exist before. Therefore, conditions (11)–(13) are checked. If necessary, the approximation step is repeated from Step 2.

As the calculations showed, the process stabilizes after 3-4 iterations.

To account for unilateral contact (separation) and friction, an algorithm has been developed, the block diagram of which is shown in Fig. 2.

The convergence process is based on the physical principle of minimizing the system's energy.

4.3. Numerical Analysis of the Stress-Strain State

Numerical studies were performed for the following system parameters:

– layer material: E_0 =1700 MPa, ν_0=0.38;

– pipe material: E_1 =200000 MPa, ν_1 =0.3;

– geometry: h = $\tilde{h}$ = 15 mm, R_1 =7 mm, R_2 =10 mm;

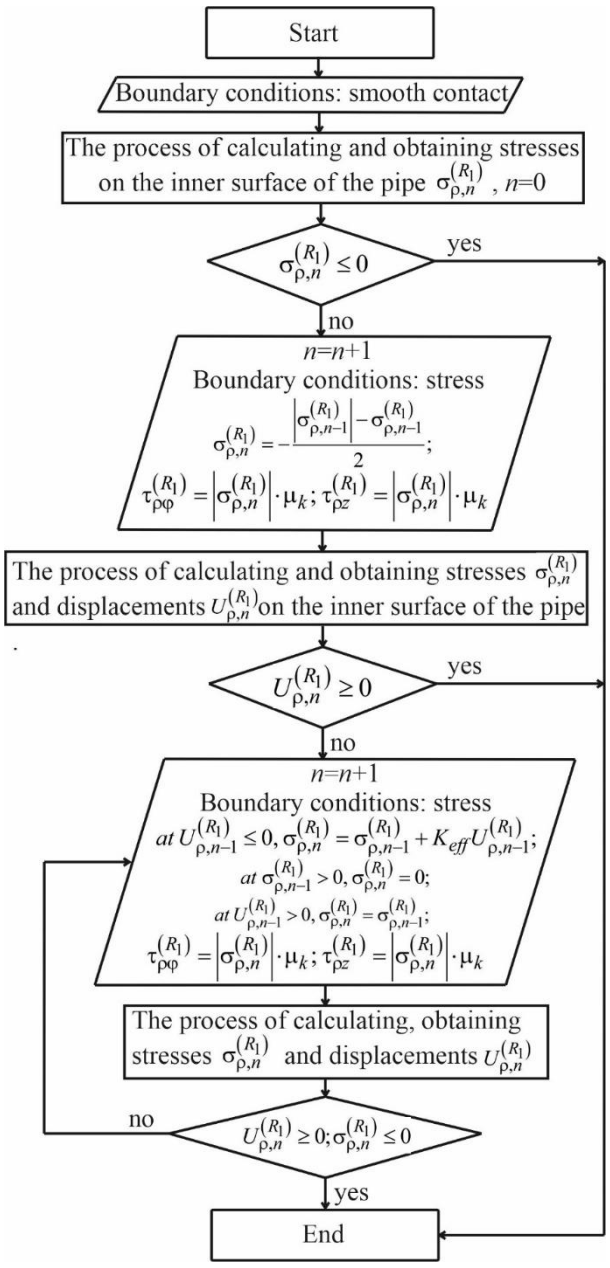

Fig. 2. Block diagram of the iterative algorithm for calculating contact interaction by alternating boundary conditions on the inner surface of the pipe

– At the upper boundary (y=h), the specified stresses act in the form of a wave, graphically represented in Fig. 1:

$$\sigma_y^{(h)}(x,z) = P \cdot 10^8 \cdot \left(z^2 + 10^2\right)^{-2} \cdot \left(x^2 + 10^2\right)^{-2},$$

$$\tau_{yx}^{(h)} = \tau_{yz}^{(h)} = 0.$$

The load intensity is calculated in two variants: P= –1; P=1; the load values P=±1 are reference values selected to demonstrate the methodology. Since the contact zone boundaries depend on the load magnitude, linear scaling of the results to other load levels is not applicable; for each specific loading scenario, the iterative procedure should be run with the actual load value.

– At the lower limit (y=$-\tilde{h}$): the conditions of rigid fixation are specified:

$$U_y^{(\tilde{h})}(x,z) = U_x^{(\tilde{h})}(x,z) = U_z^{(\tilde{h})}(x,z) = 0;$$

– At the boundary between the layer and the pipe (ρ=R_2), the conditions of ideal mechanical contact (3), (4) are satisfied;

– for the inner surface of the pipe (ρ=R_1), which is in contact with a perfectly rigid shaft, the boundary conditions are variable and depend on the stage of the iterative process. In the initial approximation, mixed conditions are specified:

$$U_0^{(R_1)}(\varphi,z) = \tau_1^{(R_1)}(\varphi,z) = \tau_2^{(R_1)}(\varphi,z) = 0;$$

– The friction coefficient is selected in 2 variants: $\mu_k = 0$; $\mu_k = 0.1$.

The infinite system was truncated at parameter m=10. At initial approximation, the accuracy of the boundary conditions was at least 10^{-5} for values from 0 to 1.

As a result of three iterations under compression (P=–1) and without taking friction into account ($\mu_k = 0$), the stresses (Table 1) and displacements (Table 2) were obtained on the inner surface of the pipe.

Table 1. Stresses by iterations at P= –1, $\mu_k = 0$

Angle, (rad)	$\sigma_{\rho,n}^{(R_1)}$, (MPa)			
	n=0	n=1	n=2	n=3
0	0.067572	-0.00111	-0.00185	-0.00245
0.785	-0.29182	-0.2924	-0.36402	-0.36408
1.570	-1.08848	-1.08887	-1.21124	-1.21106
2.356	-0.29182	-0.29241	-0.36401	-0.36395
3.141	0.067572	-0.00112	-0.00183	-0.00253
3.926	0.06548	-0.00062	-0.00110	-0.00136
4.712	0.060099	0.001091	0.001182	0.000763
5.497	0.065467	-0.0006	-0.00108	-0.00132

Table 2. Displacements by iterations at P= –1, $\mu_k = 0$

Angle, (rad)	$U_{\rho,n}^{(R_1)} \cdot 10^{-5}$, (mm)		
	n=1	n=2	n=3
0	1.85434	-1.48807	0.025401
0.785	-3.54871	3.58661	-0.02155
1.570	-6.12811	7.78262	-0.05100
2.356	-3.54884	3.5849	-0.02265
3.141	1.85403	-1.49062	0.024056
3.926	4.14534	-2.0248	0.024838
4.712	3.91157	-1.43643	0.016031
5.497	4.14567	-2.02315	0.025476

Taking into account friction ($\mu_k = 0.1$), the stresses are presented in Table 3.

Table 3. Stresses by iterations at P= –1 and $\mu_k = 0.1$

Angle, (rad)	$\sigma_{\rho,n}^{(R_1)}$, (MPa)			
	n=0	n=1	n=2	n=3
0	0.06757	-0.0012	-0.00335	-0.000591
0.785	-0.2918	-0.2923	-0.29264	-0.295704
1.570	-1.08847	-1.0888	-1.208525	-1.209808
2.356	-0.29182	-0.29244	-0.472780	-0.5965
3.141	0.06757	-0.0011	-0.044844	-0.1595883
3.926	0.06548	-0.00052	-0.005608	-0.0382022
4.712	0.06009	0.00105	-0.00075	-0.018607
5.497	0.065468	-0.00062	0.0020766	0.00237338

Taking into account friction ($\mu_k = 0.1$), the displacements are presented in Table 4.

Table 4. Displacements by iterations at P= –1, $\mu_k = 0.1$

Angle, (rad)	$U_{\rho,n}^{(R_1)} \cdot 10^{-5}$, (mm)		
	n=1	n=2	n=3
0	1.85434	-1.48807	0.025401
0.785	-3.54871	3.58661	-0.02155
1.570	-6.12811	7.78262	-0.05100
2.356	-3.54884	3.5849	-0.02265
3.141	1.85403	-1.49062	0.024056
3.926	4.14534	-2.0248	0.024838
4.712	3.91157	-1.43643	0.016031
5.497	4.14567	-2.02315	0.025476

A comparison of these stresses at $\mu_k = 0$ and $\mu_k = 0.1$ is shown in Fig. 3.

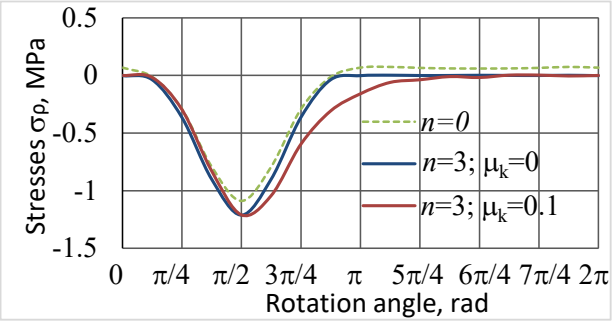

Fig. 3. Stresses $\sigma_{\rho,n}^{(R_1)}$ at P= –1

After taking into account the separation, the maximum negative stresses on the inner surface of the pipe increase (Fig. 3).

The friction coefficient also increases the compression zone. At the same time, comparing the exact values from Table 1 and Table 3, the maximum negative stresses decrease slightly.

The results of numerical calculations for tension and for the case without friction are presented in Tables 5 and 6.

Table 5. Stresses by iterations at P=1 and $\mu_k = 0$

Angle, (rad)	$\sigma_{\rho,n}^{(R_1)}$, (MPa)			
	n=0	n=1	n=2	n=3
0	-0.06757	-0.06987	-0.414792	-0.415884
0.785	0.291816	-0.0009	-0.003395	-0.007592
1.570	1.088508	0.00068	0.000437	0.000105
2.356	0.291816	-0.0008	-0.003408	-0.00726
3.141	-0.06757	-0.06823	-0.41577	-0.41578
3.926	-0.06545	-0.06641	-0.545567	-0.54854
4.712	-0.0601	-0.05903	-0.415419	-0.41757
5.497	-0.06546	-0.06605	-0.54555	-0.5486

Table 6. Displacements by iterations at P= 1, $\mu_k = 0$

Angle, (rad)	$U_{\rho,n}^{(R_1)} \cdot 10^{-5}$, (mm)		
	n=1	n=2	n=3
0	-17.1219	-4.80196	-0.60748
0.785	28.3766	-0.54662	-0.04108
1.570	64.1391	15.7857	14.9583
2.356	28.3766	-0.54703	-0.03676
3.141	-17.1217	-4.80159	-0.60681
3.926	-23.8636	9.0172	8.91897
4.712	-18.0192	13.7413	13.6402
5.497	-23.8635	9.01661	8.91863

Taking into account friction ($\mu_k = 0.1$), the stresses $\sigma_{\rho,n}^{(R_1)}$ and displacements $U_{\rho,n}^{(R_1)}$ are presented in Tables 7 and 8.

Table 7. Stresses by iterations at P= 1 and $\mu_k = 0.1$

Angle, (rad)	$\sigma_{\rho,n}^{(R_1)}$, (MPa)			
	n=0	n=1	n=2	n=3
0	-0.06758	-0.06893	-0.430894	-0.568426
0.785	0.291824	-0.00113	-0.00277	-0.07872
1.570	1.088476	-0.00024	-0.000188	-0.000107
2.356	0.291816	-0.00078	-0.004455	-0.006601
3.141	-0.06756	-0.06902	-0.398812	-0.396531
3.926	-0.06546	-0.06626	-0.537962	-0.539741
4.712	-0.06009	-0.05853	-0.415382	-0.418408
5.497	-0.06547	-0.06623	-0.553105	-0.625545

Table 8. Displacements by iterations at P= 1, $\mu_k = 0.1$

Angle, (rad)	$U_{\rho,n}^{(R_1)} \cdot 10^{-5}$, (mm)		
	n=1	n=2	n=3
0	-17.87	-9.06706	3.21459
0.785	27.7672	-4.51208	1.131348
1.570	64.14	15.6214	11.54769
2.356	28.9867	3.18581	-0.23706
3.141	-16.3742	-5.2602	-0.49026
3.926	-23.4527	11.1639	6.446378
4.712	-18.0163	13.8825	13.6144
5.497	-24.2743	7.0935	15.29302

Accounting for separation under tension significantly changes the distribution of the stress state (Fig. 4). A significant predominance due to the specified tensile stresses at free detachment leads to significant displacements in the first approximation (Table 6, Table 8). Unlike compression (Table 2, Table 4), stabilization of displacements during tension occurs only in the fourth approximation.

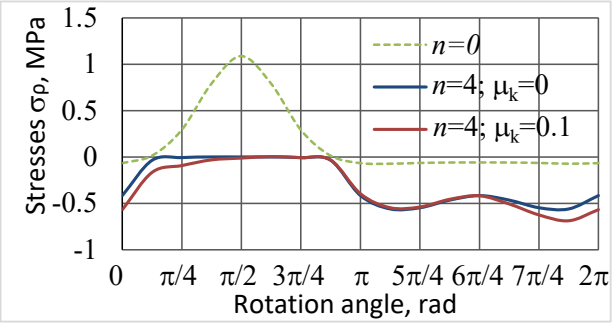

Fig. 4. Stresses $\sigma_{\rho,n}^{(R_1)}$ at P= 1

A non-zero friction coefficient also makes significant adjustments to the stress-strain state (Tables 7 and 8).

4.4. Analysis of the Convergence of the Iterative Algorithm

Analysis of the numerical data presented in Tables 1–8 allows quantitative conclusions to be drawn about the convergence rate and stability of the developed iterative algorithm.

1. Load case P=−1 (Tables 1–4).

For this type of load, the algorithm demonstrates a high convergence rate. As can be seen from Table 1 (without friction, $\mu_k = 0$), stabilization of the stress state in the main contact zone (φ =1.57 rad) is achieved already at the third iteration.

The relative difference in the values of radial stress $\sigma_{\rho,n}^{(R_1)}$ between the second and third iterations is only:

$$\delta = \left| \frac{-1,211067 - (-1,211248)}{-1,211067} \right| \cdot 100\% \approx 0,015\% .$$

This indicates that high calculation accuracy has been achieved with a minimum number of steps.

The introduction of friction (Tables 3 and 4) slightly slows down the process, but the algorithm remains stable. The difference in stress between n=2 and n=3 in the maximum load zone is about 0.1% (−1.2085 MPa vs. −1.2098 MPa), which is quite acceptable for engineering calculations.

2. Load case P=1 (Tables 5–8).

This case illustrates the operation of the contact zone correction mechanism.

Table 5 (without friction) shows how the method effectively refines the stresses. For example, at point φ =0, the stresses stabilize from –0.4148 MPa (n=2) to –0.4159 MPa (n=4), which gives an error of less than 0.26%. Fig. 5 shows the convergence of displacement and stress at points φ =0 and φ =π/2.

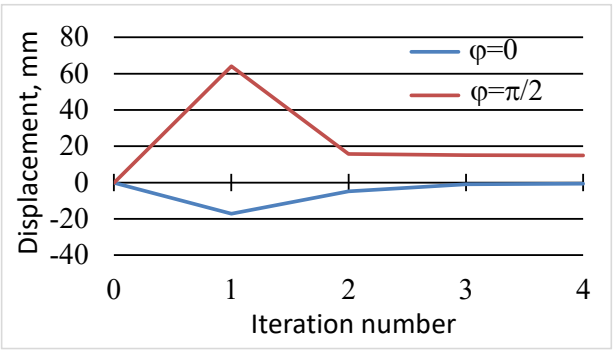

(a)

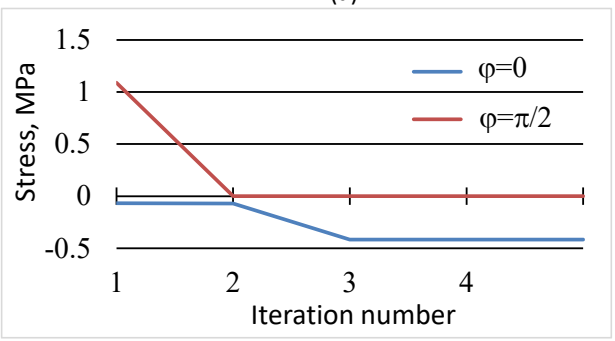

(b)

Fig. 5. Displacements $U_{\rho,n}^{(R_1)}$ (a) and stresses $\sigma_{\rho,n}^{(R_1)}$ (b) at P= 1, $\mu_k = 0$ by iterations

Table 8 (with friction) demonstrates the importance of the iterative approach for kinematic parameters. Thus, the displacement at the point φ = 0 at the second iteration was $-9.06 \cdot 10^{-5}$ mm (penetration), and at the fourth iteration it was corrected to $+3.21 \cdot 10^{-5}$ mm. This confirms that the algorithm successfully eliminates physically incorrect "penetration" of materials, ensuring that the conditions of non-penetration are met even in the presence of friction forces.

In the final iterations, slight negative values of displacements (or positive stresses) may be observed at the boundary points of the contact zone. Since their magnitude is two orders of magnitude smaller than the maximum displacements, they are considered insignificant and are treated as zero within the limits of computational accuracy.

5. DISCUSSION OF THE RESULTS

The use of the generalized Fourier method, which yields highly accurate results at each iteration, enabled the computation of stress and displacement fields while ensuring high computational accuracy. This is confirmed by the smoothness of the obtained stress distributions (Figs. 3 and 4) and the absence of oscillations characteristic of finite element models in singularity zones.

Analysis of the data presented in Tables 1–4 indicates rapid stabilization of the solution (in 2–3 iterations) for the case of predominant compression (P=−1). This is explained by the local nature of the separation zones. On the other hand, for the case of tension (P=1), as can be seen from Tables 5–8, the convergence process takes longer (stabilization at the 4^{th} iteration), which is explained by significant displacements during "free" shaft separation and the need for a significant redistribution of contact pressure to achieve equilibrium.

Fig. 3 shows that accounting for separation increases maximum compressive stresses due to the reduced effective bearing area. Additionally, the inclusion of friction (Tables 1 and 3) alters the contact zone size and the tangential stress distribution, confirming the significant impact of tribological parameters on the assembly's stress-strain state.

The fundamental difference from research [29] and [32] is the rejection of simplified assumptions about the integrity of the connection and the absence of friction. Taking into account the possibility of unilateral contact and slippage allows for a more reliable picture of the stress state to be obtained and identifies critical areas that remain underestimated when using the approach [32].

The developed iterative algorithm addresses the challenge of computing multi-connected regions by reducing the complex nonlinear contact problem to a sequence of linear problems. Unlike previous simplified approaches, this method explicitly accounts for geometric complexity and physical nonlinearities (e.g., friction, separation) without compromising the problem's geometry.

Limitations of the study: The obtained dependencies are valid within the limits of elastic material behavior. Under loads that cause plastic deformations, the results can only be used to estimate the onset of flow. The model assumes perfectly smooth contact surfaces. In real bearing bushings, surface roughness modifies the local contact pressure distribution at the asperity scale; however, for roughness amplitudes small relative to the bushing radius, the present smooth-surface solution provides a valid approximation of the mean contact pressure distribution.

6. CONCLUSION

The developed analytical-numerical approach significantly enhances the accuracy of stress-strain analysis in "elastic layer–pipe–shaft" systems by strictly accounting for non-ideal contact conditions without resorting to geometric simplifications. It was established that neglecting unilateral contact and frictional forces leads to a critical underestimation of peak stresses, as the effective bearing area decreases during surface separation. Practically, this methodology provides a robust analytical tool for assessing the strength of sliding bearing assemblies — including press-fit bushings in polymer and composite housings used in aircraft and mechanical engineering structures — where standard full-contact models critically underestimate peak stresses due to a reduction in the effective bearing area. The proposed model provides a foundation for future parametric optimization of geometric parameters, such as bushing wall thickness and housing stiffness, to extend the service life of bearing nodes under cyclic transverse loading.

Further research will focus on integrating the obtained stress distributions into fatigue life prediction models to estimate the reliability of sliding bearing assemblies. Specifically, future work aims to develop a methodology for calculating wear rates and predicting the initiation of contact fatigue cracks, taking into account the non-stationary nature of the contact zone boundaries identified in this study.

CONFLICTS OF INTEREST

The authors declare no conflict of interest.

REFERENCES

[1] European Commission, Flightpath 2050: Europe's Vision for Aviation. Report of the High Level Group on Aviation Research. *Publications Office of the European Union*, Luxembourg, 2011. https://op.europa.eu/en/publication-detail/-/publication/296a9bd7-fef9-4ae8-82c4-a21ff48be673 (Accessed: 5 January 2026)

[2] A.V. Kondratiev, V.O. Kovalenko, Optimization of design parameters of the main composite fairing of the launch vehicle under simultaneous force and thermal loading. *Space Science and Technology*, 25(4), 2019: 3–21. https://doi.org/10.15407/knit2019.04.003

[3] A. Kondratiev, Improving the mass efficiency of a composite launch vehicle head fairing with a sandwich structure. *Eastern-European Journal of Enterprise Technologies*, 6(7), 2019: 6–18. https://doi.org/10.15587/1729-4061.2019.184551

[4] A. Kondratiev, V. Píštěk, V. Gajdachuk, M. Kharchenko, T. Nabokina, P. Kučera, O. Kučera, Effect of ply orientation on the mechanical performance of carbon fiber honeycomb cores. *Polymers*, 15(11), 2023: 2503. https://doi.org/10.3390/polym15112503

[5] M. Vicen, O. Bokůvka, L. Trško, R. Joch, J. Bronček, R. Nikolić, R. Ulewicz, Influence of the Surface Roughness, Lubrication and Grinding on Tribological Properties of the C35 Steel Shot-Peened Surfaces. *Applied Engineering Letters*, 9(4), 2024: 185-194. https://doi.org/10.46793/aeletters.2024.9.4.1

[6] K.L. Johnson, Contact Mechanics. *Cambridge University Press*, Cambridge, 1985. https://doi.org/10.1017/CBO9781139171731

[7] V. Quaglini, P. Dubini, D. Ferroni, C. Poggi, Influence of counterface roughness on frictional properties of engineering plastics for bearing applications. *Materials & Design*, 30(5), 2009: 1650–1658. https://doi.org/10.1016/j.matdes.2008.07.025

[8] N. Menga, C. Putignano, G. Carbone, G.P. Demelio, The sliding contact of a rigid wavy surface with a viscoelastic half-space. *Proceedings of the Royal Society A*, 470, 2014: 20140392. https://doi.org/10.1098/rspa.2014.0392

[9] L. Ivanović, B. Rakić, B. Stojanović, M. Matejić, Comparative Analysis of Analytical and Numerical Calculations of Contact Stresses at Rotational Elements of Gerotor Pumps. *Applied Engineering Letters*, 1(1), 2016: 1-7.

[10] P. Gontarovskyi, N. Smetankina, N. Garmash, I. Melezhyk, Numerical analysis of stress-strain state of fuel tanks of launch vehicles in 3D formulation. *Integrated Computer Technologies in Mechanical Engineering - 2020*. *Lecture Notes in Networks and Systems*, 188, 2021: 609–619. https://doi.org/10.1007/978-3-030-66717-7_52

[11] V. Golovanevskiy, A. Kondratiev, Elastic properties of steel-cord rubber conveyor belt. *Experimental Techniques*, 45(2), 2021: 217–226. https://doi.org/10.1007/s40799-021-00439-3

[12] P.P. Gontarovskyi, N.V. Smetankina, N.G. Garmash, I.I. Melezhyk, T.V. Protasova, Three-Dimensional Stress-Strain State Analysis of the Bimetallic Launch Vehicle Propellant Tank Shell. *Strength of Materials*, 55, 2023: 916-926. https://doi.org/10.1007/s11223-023-00582-9

[13] M. Jafari, M.H.B. Chaleshtari, H. Khoramishad, H. Altenbach, Minimization of thermal stress in perforated composite plate using metaheuristic algorithms WOA, SCA and GA. *Composite Structures*, 304, 2023: 116403. https://doi.org/10.1016/j.compstruct.2022.116403

[14] A. Toselli, O.B. Widlund, Domain Decomposition Methods — Algorithms and Theory. *Springer*, Berlin, Heidelberg, 2005. https://doi.org/10.1007/b137868

[15] P.A. Boucard, P. Ladevèze, A multiple solution method for non-linear structural mechanics. *Mechanical Engineering*, 50, 1998: 317–328.

[16] C. Farhat, F.X. Roux, Implicit Parallel Processing in Structural Mechanics. Computational Mechanics Advances, 2(1), 1994: 1-124.

[17] S.N. Atluri, S. Shen, The Meshless Local Petrov-Galerkin (MLPG) Method: A Simple & Less-costly Alternative to the Finite Element and Boundary Element Methods. *Computer Modeling in Engineering & Sciences*, 3(1), 2002: 11-51. https://doi.org/10.3970/cmes.2002.003.011

[18] T. Belytschko, Y. Krongauz, D. Organ, M. Fleming, P. Krysl, Meshless methods: An overview and recent developments. *Computer Methods in Applied Mechanics and Engineering*, 139(1-4), 1996: 3-47. https://doi.org/10.1016/S0045-7825(96)01078-X

[19] A.V. Zasovenko, A.V. Fasolyak, Mathematical modeling of the dynamics of an elastic half-space with a cylindrical cavity reinforced by a shell under axisymmetric loads. *New materials and Technologies in Metallurgy and Mechanical Engineering*, (2), 2023: 67–73.

https://doi.org/10.15588/1607-6885-2023-2-10

[20] P. Malits, Torsion of an elastic half-space with a cylindrical cavity by a punch. *European Journal of Mechanics - A/Solids*, 89, 2021: 104308. https://doi.org/10.1016/j.euromechsol.2021.104308

[21] V.V. Meleshko, Yu.V. Tokovyy, Equilibrium of an elastic finite cylinder under axisymmetric discontinuous normal loadings. *Journal of Engineering Mathematics*, 78, 2013: 143–166. https://doi.org/10.1007/s10665-011-9524-y

[22] A.A. Fesenko, An exact solution of the dynamical problem for the infinite elastic layer with a cylindrical cavity. *Research in Mathematics and Mechanics*, 24(2), 2019: 75–87. https://doi.org/10.18524/2519-206x.2019.2(34).190054

[23] V. Nikolić, Ć. Dolićanin, M. Radojković, E. Dolićanin, Stress distribution in an anisotropy plane field weakened by an elliptical hole. *Tehnički Vjesnik*, 22(2), 2015: 329–335. https://doi.org/10.17559/TV-20131102132713

[24] M. Radojković, I. Čamagić, S. Sedmak, Influence of elliptical opening position on the distribution of minimum principal normal stress. *Structural Integrity and Life*, 23(3), 2023: 245–249.

[25] A.G. Nikolaev, V.S. Protsenko, Generalized Fourier method in spatial problems of elasticity theory. *National Aerospace University named after M.E. Zhukovsky "KHAI"*, Kharkiv, 2011, 344. (In Russian)

[26] V. Miroshnikov, Investigation of the stress state of a composite in the form of a layer and a half space with a longitudinal cylindrical cavity at stresses given on boundary surfaces. *Journal of Mechanical Engineering*, 22(4), 2019: 24–31. https://doi.org/10.15407/pmach2019.04.024

[27] N. Ukrayinets, T. Alyoshechkina, V. Miroshnikov, O. Savin, B. Younis, V. Vynohradov, O. Murahovska, Consideration of Spatially Infinite Loads in the Problem for a Layer with a Cylindrical Cavity and Continuous Supports. *Computation*, 13(11), 2025: 270. https://doi.org/10.3390/computation13110270

[28] M.M. Grebenikov, K.V. Mironov, Stress state analysis of a layer with a longitudinal cavity and given non-classical mixed boundary conditions. *XIX International Science Conference "Science, Theory and Practice"*, 8-11 June 2021, Tokyo, Japan, pp.536–540.

[29] M. Vitaly, Rotation of the Layer with the Cylindrical Pipe Around the Rigid Cylinder. *Advances in Mechanical and Power Engineering. CAMPE 2021*. *Lecture Notes in Mechanical Engineering*, 2023: 314–322. https://doi.org/10.1007/978-3-031-18487-1_32

[30] M.M. Grebennikov, K.V. Mironov, The first fundamental problem of elasticity theory for a layer with a longitudinal cylindrical thick-walled pipe. In: *XXVIII International Scientific and Practical Conference "Trends in Science and Practice of Today"*, 1-4 June 2021, Ankara, Turkey, pp.482–486.

[31] V. Miroshnikov, O. Savin, O. Denshchykov, O. Ilin, M. Kosenko, Influence of Cylindrical Gasket Material on Stress State of a Layer with Embedded Cylindrical Supports. *Integrated Computer Technologies in Mechanical Engineering - 2024*. *Lecture Notes in Networks and Systems*, 1474, 2025: 587–597. https://doi.org/10.1007/978-3-031-94852-7_50

[32] V. Miroshnikov, O. Denshchykov, I. Grebeniuk, O. Savin, An Analysis of the Stress–Strain State of a Layer on Two Cylindrical Bearings. *Computation*, 12(9), 2024: 182. https://doi.org/10.3390/computation12090182

[33] ISO 286-1:2010. Geometrical product specifications (GPS) — ISO code system for tolerances on linear sizes — Part 1: Basis of tolerances, deviations and fits. *International Organization for Standardization*, Geneva, 2010.